

Extreme high-pressure distortion phase of Bi_2MoO_6 in $\text{Bi}_2\text{Mo}_{0.94}\text{W}_{0.06}\text{O}_6$ at ambient pressure for augmented octahedral rotations and metal-oxide charge transport

Anurag Pritam^{a)} and Vaibhav Shrivastava^{a),*}

a) Dielectric Laboratory, Shiv Nadar University, Uttar Pradesh, India

Bismuth molybdate (BMO) is the simplest compound of aurivillius family with a wide range of application as a tunable capacitor and sensor. The present article deals with the study of a structural, optical and catalytic property of tungsten doped Bismuth molybdate. The crystal structure is critically studied by Rietveld structural refinement method by using X-ray powder diffraction data. Raman scattering indicates that the structural distortion in BMO is mainly due to the rigid rotation of MoO_6 octahedra. Due to the introduction of tungsten, the system experienced an increase in the band gap, which is studied by Uv-vis spectroscopy and W doped BMO show remarkable photocatalytic behavior compared to pure one.

1. Introduction

Tailoring the crystallinity and bandgap of perovskite materials has phenomenological significance owing to their numerous applications in the field of optoelectronics, memory devices, sensing, and photocatalysis. Among all materials, Bismuth molybdates (Bi_2MoO_6) serves as an ideal material with all these unique properties for LTCC technology, it is one of the simplest units of the large family of Bismuth layered structured ferroelectrics (BLSF) perovskite known since 1949.¹⁻² The structure of this compound is described by the general formula $(\text{Bi}_2\text{O}_2)^{2+} (\text{A}_{n-1}\text{B}_n\text{O}_{3n+1})^{2-}$, where A sites can be taken by mono, di or trivalent compound and B sites can be occupied by rare-earth elements and n represents the number of BO_6 octahedra in a perovskite layer ($n=1,2,3,4$ and 5).³⁻⁵ The crystal arrangement of this compound comprises of alternating Bi_2O_2 layers and perovskite-like a layer of corner linked BO_6 octahedra.³⁻⁵ Bi_2MoO_6 known as one of the most convoluted compounds of BLSF due to the polymorphic phase of its crystal structure, which can be isolated by giving optimum temperature treatment depending on its method of synthesis, each phase illustrating distinct utilization as an oxygen ionic conductor, catalytic activity and

ferroelectric materials. Three discrete phases mentioned as: at low temperature the stable phase of Bi_2MoO_6 is denoted by γ phase exhibiting fluorite-like structure, the intermediate phase is denoted by γ' which is stable till 600°C , in case of reversible transition, the γ and γ' phases show layered aurivillius type structure where perpetual arrangement of alternate (Bi_2O_2) and (MoO_4) sheets along a crystallographic axis. Recent studies by several authors indicate that the transition of γ to γ' phase in Bi_2MoO_6 is basically associated with a ferroelectric to paraelectric type transition. γ' phase is generally orthorhombic in nature rather than that of tetragonal symmetry, in few studies, it is observed that at this temperature second harmonic generation signal generally disappears from Bi_2MoO_6 hence proving that γ' is non-polar in nature. Finally, a stable, non-reversible (γ'') phase is obtained when Bismuth molybdate is heated above 670°C . The γ'' phase has a monoclinic structure with space group of $\text{P}2_1/\text{C}$, γ'' phase shows original structure due to presence of MoO_4 tetrahedra enclosing ribbons of Bi-O in place of MoO_6 octahedra which is generally revealed at lower temperature phases.⁶⁻⁷ Physical properties of the material heavily depend upon the microstructure and doping, the effect of doping on different physical and chemical properties of the solid materials is well known and this response is widely employed in ferroelectrics to enhance their performance, so therefore by controlling these parameters, one can tailor the physical properties of the materials. Rietveld's X-ray powder structure refinement has been considered in the present work because no other method is equally capable of determining the crystal structure, lattice strain, crystallite size, and atomic parameters of nanocrystalline material consists of a large number of superimposed reflections.⁸⁻⁹

In this article, we determine the usefulness of new solid solution with the general composition of $\text{Bi}_2\text{Mo}_{1-x}\text{W}_x\text{O}_6$ by solid-state route method where x varies from 0.00 to 0.10. The phase, crystallite size and lattice parameters of $\text{Bi}_2\text{Mo}_{1-x}\text{W}_x\text{O}_6$ at room temperature is observed and deliberated on the basis of X-ray diffraction (XRD) with Rietveld

refinement, the change in phonon properties of composition due to appropriate doping, variation of electronic band gap is also investigated on basis of UV-Vis spectroscopy, Raman scattering is carried out to gain evidence on structural changes occurring in the material.

2. Materials and methods

Stoichiometrically taken Bi_2O_3 , MoO_3 and WO_3 powders (All from Sigma Aldrich USA) were thoroughly grounded before microwave calcinations at 575°C for 5 hours. The range of tungsten doping in composition $\text{Bi}_2\text{Mo}_{1-x}\text{W}_x\text{O}_6$ (BMoW) was from $x=0.0$ to 0.06 with stepsize 0.01 , 0.08 and 0.10 . Eurotherm 2416 controller was used for varying microwave input power monitored through a typical pre-set thermal profile during calcinations and sintering. Detailed preparation and initial x-ray diffractograms have been reported elsewhere []. The refinement process of obtained x-ray diffraction data was carried using program Fullprof estimating P21c space group orthorhombic unit cell for prepared $\text{Bi}_2\text{Mo}_{1-x}\text{W}_x\text{O}_6$ (BMoW) compositions. The surface morphology of prepared pellets was investigated using field-emission SEM of make Carl Zeiss Merlin VP with 5kV acceleration voltage and 100KX magnification. Before recording images, pellet surfaces were coated using a thin layer of gold to avoid dipolar charging effects on surface. Microwave synthesis is the result of high frequency 2.45GHz microwaves coupled with each dipole in a material or atmosphere and generating local high temperature regions for calcinations/sintering due to dipolar switching at microwave frequencies. High-frequency treatment of starting dielectric oxide materials is For detecting transitions between vibrational energy states created for accommodating inelastic collision derived electron transfer, raman spectroscopy was deployed. These measurements were performed by exciting BMoW composition powders with He-Ne laser beam of 532nm wavelength. Scattered light was analyzed using an HR-800 Horiba JobinYvon, micro-Raman spectrophotometer having a spectral resolution of $\sim 1\text{ cm}^{-1}$ equipped with an edge filter (1800 lines/mm grating with CCD detector) for Rayleigh line rejection. Charge transfer mechanism

in all BMoW compositions was investigated using impedance spectroscopy based on room temperature dielectric dispersion data and cyclic voltammetry. Dielectric dispersion (accuracy~0.08%) was recorded using high frequency LCR meter NF2376 (NF Corporation, Japan) in frequency range from 20 Hz to 1MHz at an oscillation level of 1V oscillation. Redox investigations were carried using cyclic voltammetry (C-V) performed on Autolab Potentiostat Galvanostat PGSTAT302N (Metrohm, Netherlands). For this electrochemical characterization, CV measurements were recorded in a three-electrode set-up consisting of Ag/AgCl as the reference electrode, platinum wire as the counter electrode and glassy carbon electrode (GCE) modified with two typical BMoW ($x=0.0$ and 0.10) compositions as the working electrode. The standard electrolyte used in reaction was 5 mM of Potassium Ferro/Ferri cyanide in 0.1 M KCl. The CV scans were recorded from -0.4 V to 1 V with the scan rate of 0.50 mVs⁻¹. The *dc* conduction response of all BMoW compositions was recorded using conventional 2-probe setup connected with Keithley 6517B electrometer and Eurotherm 3216 controller based oven. The trigger voltages were varied from 1V to 10V and change in direct current was recorded with temperatures up to 300°C for determining low temperature defect/doping induced charge flow. *DC* conductivity was calculated using Ohm's law and each *dc* conduction behaviour was plotted in Arrhenius form for computing activation energy. UV-Vis spectrophotometer (Shimadzu Solid Spec-3700) was deployed for recording diffuse absorbance in an integrating sphere mode for estimating doping effects on optical energy bandgaps. Tauc plots were used for estimating optical energy bandgaps after confirming indirect band gap transition in BMoW materials.

3. Results and discussions

X-ray powder diffraction is one of the most powerful technique to obtain qualitative and microstructural information for polycrystalline materials. However, polymorphic forms of few multi-elemental ceramic matrices (sharing nearly equal lattice spacing with different

crystal symmetries) are difficult to be analysed just by using as obtained diffraction data. For such cases, the quantitative study is not possible due to difficulties in the overlapping of the different Braggs reflections making traditional x-ray diffraction method unsatisfactory. To resolve this problem, a very well established Rietveld refinement method that is a simulation program to refine the theoretical line profile by least square fitting method, is used. Various profile-fitting parameters make it very convenient to conclude exact crystal symmetry or changes in parent structure besides helping in estimating strain induced microstructure. It is practiced to know the domain size, microstructure and strain values from the refined profile width parameters. Where W_i is the weight parameter and I_{io} and I_{ic} is defined as observed and calculated intensity for diffraction angles $2\theta_i$. Other important parameters like profile residual (R_p) and weighted profile (R_{wp}) which is basically the measure of the degree of difference of calculated and observed values, is depicted below,¹¹⁻¹⁴

$$\Delta = \sum_i W_i \{I_{io} - I_{ic}\}^2$$

$$R_p = \frac{\sum_i |I_{io} - I_{ic}|}{\sum_i I_{io}}$$

$$R_{wp} = \left[\frac{\sum_i W_i (I_{io} - I_{ic})^2}{\sum_i W_i \{I_{io}\}^2} \right]^{1/2}$$

Fig.1 shows the Rietveld refined XRD patterns of polycrystalline $Bi_2Mo_{1-x}W_xO_6$ (for $x=0.0$ and 0.06). The diffraction patterns were indexed assuming orthorhombic unit cell structure with space group $P2_1/c$. Excellent fitting can be seen through a close overlap between observed and calculated intensity values. This confirms the correctness of presumed orthorhombic unit cell structure and induces to explore exact structure of unit cell before and after doping. The profile matching indicates that unit cell remains unchanged post tungsten doping in place of molybdenum in octahedron cages. Refined derived atomic coordinates, listed in Table-1, were further used to obtain wyckoff positions of each atom using Bilbao

crystallographic server. All atomic coordinates indicate expected *8b*wycoff positions occupied by Bi, Mo/W and O ions.

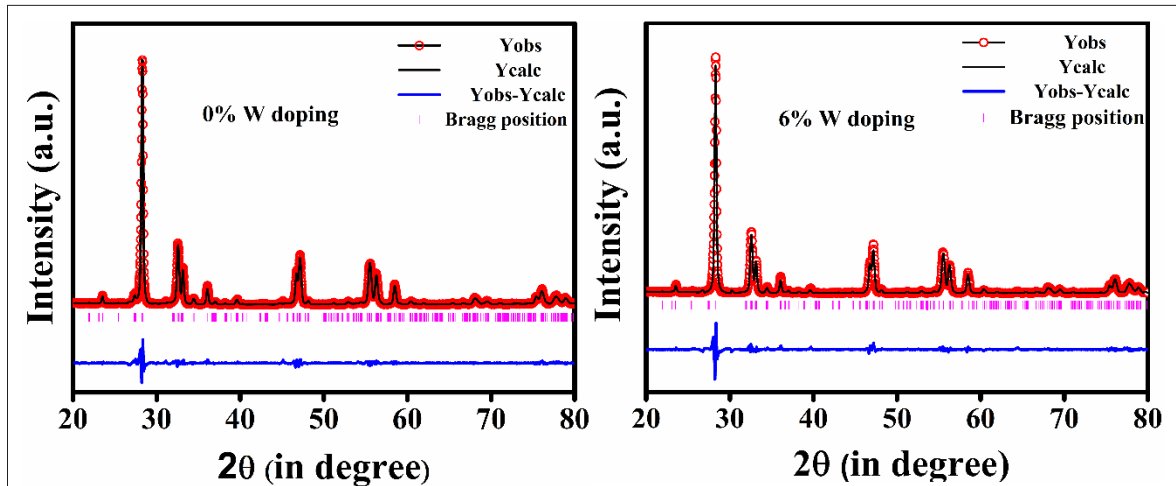


Fig. 1. Rietveld refinement patterns of Bi_2MoO_6 and $\text{Bi}_2\text{Mo}_{0.94}\text{W}_{0.06}\text{O}_6$.

Table-1 Change in atomic positions on doping in $\text{Bi}_2\text{Mo}_{1-x}\text{W}_x\text{O}_6$ (with refined Wyckoff positions).

Atom coordinates (Wyckoff position)	Bi_2MoO_6	$\text{Bi}_2\text{Mo}_{0.94}\text{W}_{0.06}\text{O}_6$	$\text{Bi}_2\text{Mo}_{0.90}\text{W}_{0.10}\text{O}_6$
Bi(1) (8b)			
X	0.5242	0.5199	0.5204
Y	0.4208	0.4220	0.4245
Z	0.9945	0.9205	1.0413
Bi(2) (8b)			
X	0.4849	0.4816	0.4876
Y	0.0765	0.0786	0.0816
Z	0.9916	0.9167	1.0559
Mo(1)/W(1) (8b)			
X	-0.0076	0.0080	0.0158
Y	0.2465	0.2459	0.2482
Z	0.0116	0.0707	0.0183
O(1) (8b)			
X	0.0196	0.0216	0.0266
Y	0.1446	0.1406	0.1291
Z	0.0901	0.0258	0.1327
O(2) (8b)			
X	0.2290	0.2986	0.3771
Y	1.009	0.9873	1.0486
Z	0.2659	0.2875	0.1796
O(3) (8b)			
X	0.2872	0.2811	0.1860

Y	0.5255	0.5026	0.5204
Z	0.3194	0.2150	0.3617
O(4) (8b)			
X	0.7326	0.7501	0.6570
Y	0.2226	0.2260	0.2531
Z	0.2861	0.2263	0.4205
O(5) (8b)			
X	0.2494	0.2060	0.1847
Y	0.3242	0.2769	0.2910
Z	0.5670	0.2942	0.3610
O(6) (8b)			
X	0.6187	0.6311	0.6368
Y	0.3834	0.3335	0.3522
Z	0.5453	0.5221	0.6983

Absence of *4awycoff* positions in all prepared BMoW materials confirm the formation of first layer Aurvillius phase formation on doping. The refined unit cell parameters and profile reliability parameters for each BMoW composition are listed in Table-2. A marginal deviation in the values of statistical parameters R_p , R_{wp} and R_{exp} for all doped BMoW compositions compared to undoped BMo composition establishes the following, *a*) absence of any undesired polluting phase throughout *evendoping* range and *b*) unchanged orthorhombic unit cell in all BMoW compositions¹⁵. Careful comparative analysis of experimentally obtained lattice parameters with those refined indicates prominent *a-b* plane octahedral rotations on tungsten doping than *a-c* plane tilting of the same, Table-3. This induces further in-depth study of

Table-2 Unit cell parameters and reliability factors for Rietveld refined doped $\text{Bi}_2\text{Mo}_{1-x}\text{W}_x\text{O}_6$ crystal structure

Parameters	a (Å)	b (Å)	c (Å)	R_p (%)	R_{wp} (%)	R_{exp}
x=0.00	5.485	16.209	5.507	12.4	15.8	8.03
x=0.02	5.487	16.213	5.508	15.3	18.1	9.9
x=0.04	5.485	16.216	5.5066	14.3	19.1	8.64
x=0.06	5.484	16.219	5.507	10.72	13.2	4.68

x=0.08	5.484	16.217	5.508	15.2	17.7	9.77
x=0.10	5.484	16.217	5.509	13.9	17	8.7

Table-3 Unit cell parameter variation in Bi₂Mo_{0.94}W_{0.06}O₆ before and after refinement.

Parameters	Before Rietveld Refinement	After Rietveld Refinement
a (Å)	5.406	5.4839
b (Å)	16.509	16.2177
c (Å)	5.503	5.5056

tungstendoping caused changes in bond angles of BMo unit cells, Table-4, and leads for the designing of unit cell structure as shown in Fig.2. Tungsten [Xe: $5d^4$, $6s^2$] intrinsically possess lesser electron-electron repulsions than Molybdenum [Kr: $4d^5$, $5s^1$] having more diffused charge distribution. This renders a vacant $5^{th}d$ -orbital ($d_{x^2-y^2}$) in tungsten compared to molybdenum generating more free rattling space in a - b plane. Hence, Mo/W bonds with selective oxygen's (e.g. O1, O4, O5 and O6) show significant rotations than the others (O2 and O3). This is indicated in Fig.2, where octahedrons MoO₆/WO₆ appear to rotate significantly along $-c$ - b plane clockwise and in complementary manner towards each other (O1, O4 and O5 can be prominently seen to re-aligned by octahedral tilting) [R.G.Teller, ActaCryst paper, 1984]. Therefore, tungsten doping in BMo matrix induces octahedral tilting to keep oxygen ions away from open surfaces designing these surfaces typically oxygen free for any surface driven effect.

Table-4 Change in bond angles with doping in Bi₂Mo_{1-x}W_xO₆ (all values are in degrees).

Atom	x=0.0	x=0.06
Bi2-O1-Mo1/W1	40.7035	58.7880
O6-Mo1-O4	102.574	69.2969
O1-Bi1-Mo1	49.7476	16.5515
Bi1-Mo1-O5	105.2259	80.0790

W1/Mo1-Bi1-O6	150.9642	32.1484
W1/Mo1-Bi2-O2	145.9537	142.9503
W1/Mo1-Bi2-O5	33.3456	42.8488

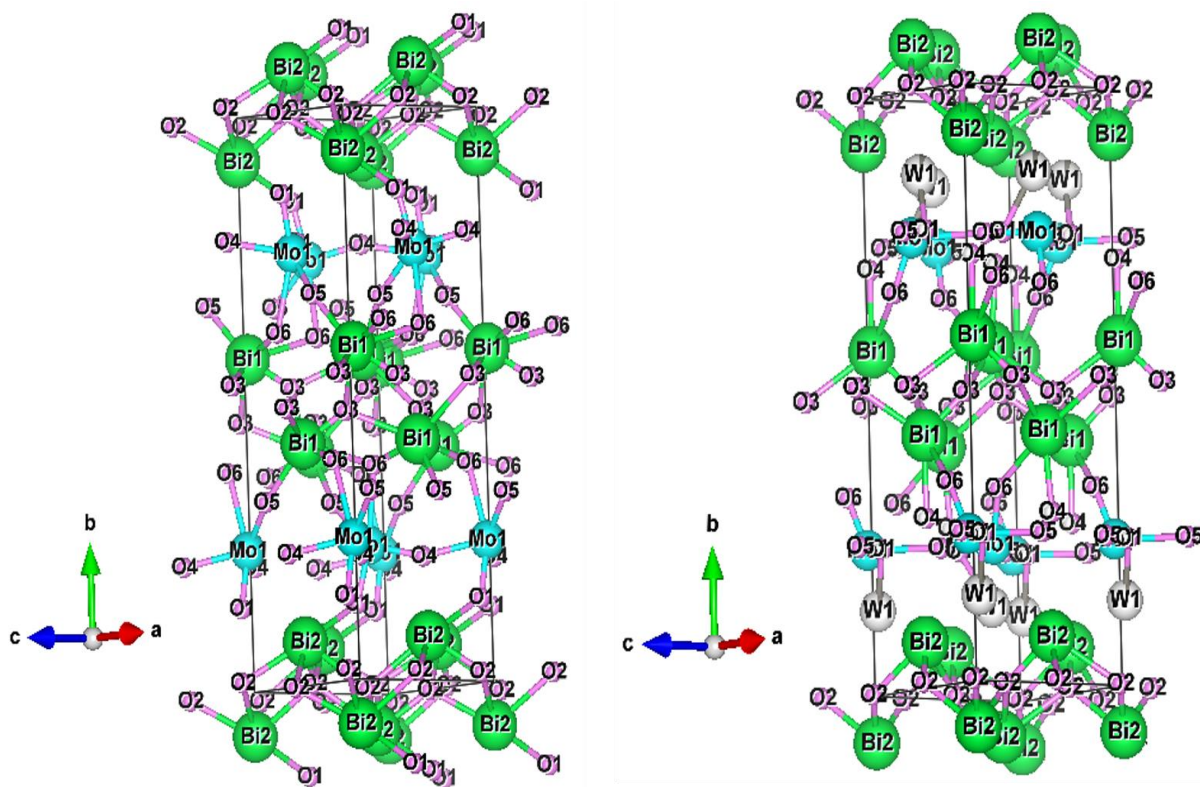


Fig.2. Crystal structure of Bi₂MoO₆ (x=0.0) and Bi₂Mo_{0.94}W_{0.06}O₆ (x=0.06)

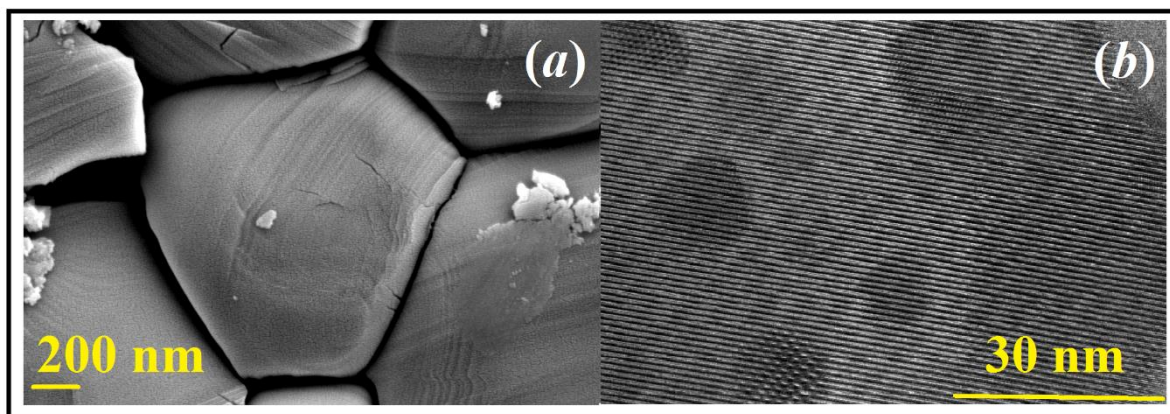


Fig.3 Grain distribution and nanoparticle formation in pure Bi_2MoO_6

Hydraulically compacted and microwave sintered (at 595°C for 2hrs) pellet surface of Bi_2MoO_6 composition has been shown in Fig.3(a) using field-emission SEM micrographs. An interesting hexagonal grain formation with *alternately arranged* equal dimensions. Such a continuous grain formation occurs in powders with schematically distributed pores usually derived in microwave synthesis []. All grains have edge-to-edge dimension of $1.8\mu\text{m}$, that is very well within standard range ($1\text{-}2.5\mu\text{m}$) of grain size in bismuth layer materials due to bismuth oxide loss from grain connecting surfaces during sintering to coalesce grains in better manner []. Average grain size is estimated to be $3\mu\text{m}$ using ImageJ software that presumably incorporates width of darker void boundaries into estimation. Fig.3(b) depicts the TEM image of crushed pellet, hexagonal nano particles (size $\sim 15\text{-}20\text{nm}$) grown on regular atomic network can be seen. Such juttred out nano particles are overall dispersed on micro sized grains possibly due to trapping of microwaves between molybdenum-sites of gross network acting as *susceptors*. Microwaves trapped between these sites heat the region excessively and major bismuth oxide region swallows towards surface taking all interior planes of Mo/W-oxides together.

Apart from XRD, Raman scattering investigations help crucially in determining, *a)* phase purity, *b)* effect of dopant on modifying local vibrational behaviour of metal-oxygen bonds

(like stretching/bending/wagging) and *c*) finally electronic shell deformation effect on intrinsic electric dipole moment. Raman spectra of typically chosen $\text{Bi}_2\text{Mo}_{1-x}\text{W}_x\text{O}_6$ compositions is shown in Fig.4, all expected raman bands are observed. Intensity of the raman bands change optimally with tungsten doping in $\text{Bi}_2\text{Mo}_{1-x}\text{W}_x\text{O}_6$ matrix. Raman spectra is a close fingerprint of polymorphic structural changes that occur in Bi_2MoO_6 and Bi_2WO_6 materials mostly due to the rigid rotations of MoO_6/WO_6 octahedrons [Maczka PRB (2008), Maczka J.Phys.:Condensed Matter (2010)]. Raman bands observed above 600cm^{-1} belong to the Mo-O stretching and below 400cm^{-1} to bending, wagging and external translational motion of Bi- and Mo-ions. Intense raman bands observed around 793cm^{-1} and 850cm^{-1} in present work are

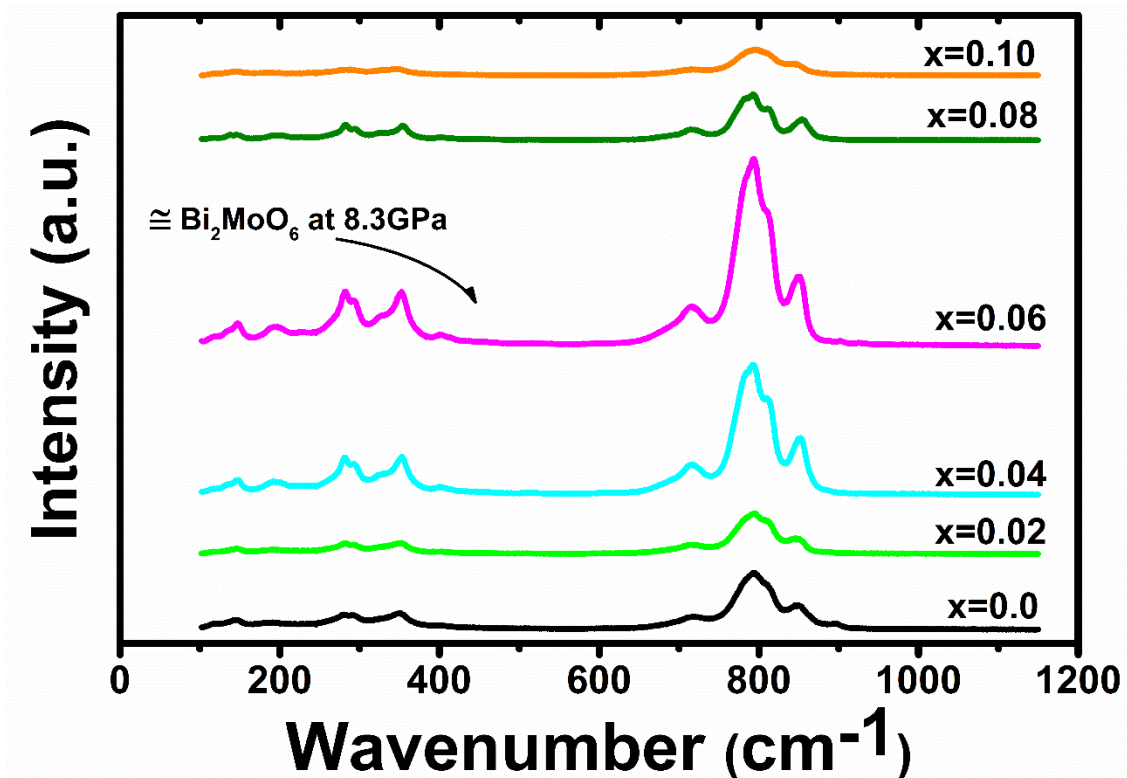


Fig.4 Raman spectra of $\text{Bi}_2\text{Mo}_{1-x}\text{W}_x\text{O}_6$ compositions recorded at 25°C and 0.0001GPa

corresponding to symmetric (A_{1g} mode) and asymmetric ($A_{2u}+E_u$ mode) stretching of the MoO_6/WO_6 octahedrons. Both of these modes emerge as non-centrosymmetric and polar due to intrinsic structural distortions in MoO_6 octahedrons partly compensated by larger

electronic cloud of tungsten (W). Additional bands in the range $690\text{-}720\text{cm}^{-1}$ are due to the asymmetric stretching mode of MoO_6 octahedra via motion of equatorial oxygen ions connecting these octahedra with Bi_2O_2 layers. The bending modes for bismuth oxide polyhedral connected with MoO_6 octahedra are observed from $180\text{-}500\text{cm}^{-1}$. Raman active doubly degenerate (E_g) modes due to rocking of the octahedra are observed from 270cm^{-1} to 360cm^{-1} . Optimum 6% tungsten doping in $\text{Bi}_2\text{Mo}_{1-x}\text{W}_x\text{O}_6$ matrix at ambient pressure (0.0001 GPa) and temperature (25°C) generates non-centrosymmetric polar orthorhombic structure identical to the Bi_2MoO_6 matrix prepared under extreme high pressure ($\sim 8.3\text{GPa}$) using diamond anvil setup. Tungsten doping beyond 6% is observed to saturate polar character of $\text{Bi}_2\text{Mo}_{1-x}\text{W}_x\text{O}_6$ unit cell and larger electronic cloud of tungsten starts shielding intrinsic dipoles to result into less polar or more symmetric unit cell possibly in tetragonal space group $I4/mmm$ [R.L. Withers J. Solid State Chem, 1991].

Complex Impedance spectroscopy (CIS) is an effective tool that can resolve electronic conduction deriving from all possible sources like grain, grain boundaries and grain-electrode interface in applied electric input frequency domain. Nyquist plots ($Z'-Z''$) are used in determining conduction from major grain resistance part of the material though not sensitive towards conduction corresponding to smaller values of resistance due to grain boundary and electrode-material interface. This low resistance conduction mechanism is explained by complex modulus plot ($M'-M''$). Fig. 5 shows the room temperature complex impedance plot for doped $\text{Bi}_2\text{Mo}_{1-x}\text{W}_x\text{O}_6$ materials investigated from 100 Hz to 1 MHz. Bulk grain resistance values for tungsten-doped $\text{Bi}_2\text{Mo}_{1-x}\text{W}_x\text{O}_6$ samples are sufficiently lower than undoped Bi_2MoO_6 material. Tungsten doping $\sim 2\%$ was able to curtail lossy behaviour of pure Bi_2MoO_6 material that shows non-Debye tail at low frequencies. This is due to comparatively large resistive-capacitive grain boundary exhibiting multiple relaxation times. All tungsten-doped $\text{Bi}_2\text{Mo}_{1-x}\text{W}_x\text{O}_6$ samples show nearly an ideal Debye behaviour with centres of all

semicircles well above Z' -axis and emerging 2nd semicircle optimally around 4-6% tungsten doping. For samples doped beyond 6%, the 2nd semicircle emerges again and becomes wider. Fig.6 shows the frequency dispersion of Z' and Z'' for $\text{Bi}_2\text{Mo}_{1-x}\text{W}_x\text{O}_6$ materials. Real impedance Z' for all tungsten doped samples decreases to nearly 10% of its value for undoped Bi_2MoO_6 sample. Overall, it is minimum for 2% tungsten doping and maximum for undoped Bi_2MoO_6 . The distribution of Z' -curves before 10^3Hz is in order of space charge magnitude in $\text{Bi}_2\text{Mo}_{1-x}\text{W}_x\text{O}_6$ materials that saturates quickly beyond 10^5Hz irrespective of tungsten concentration. In accordance with Z' -behaviour, Z'' -peaks shift regularly towards low frequencies till 8% tungsten doping in $\text{Bi}_2\text{Mo}_{1-x}\text{W}_x\text{O}_6$ materials indicating maximum loss of energy at resonance due to low frequency responsive space charge accumulating at grain boundaries and inhibiting charge transfer

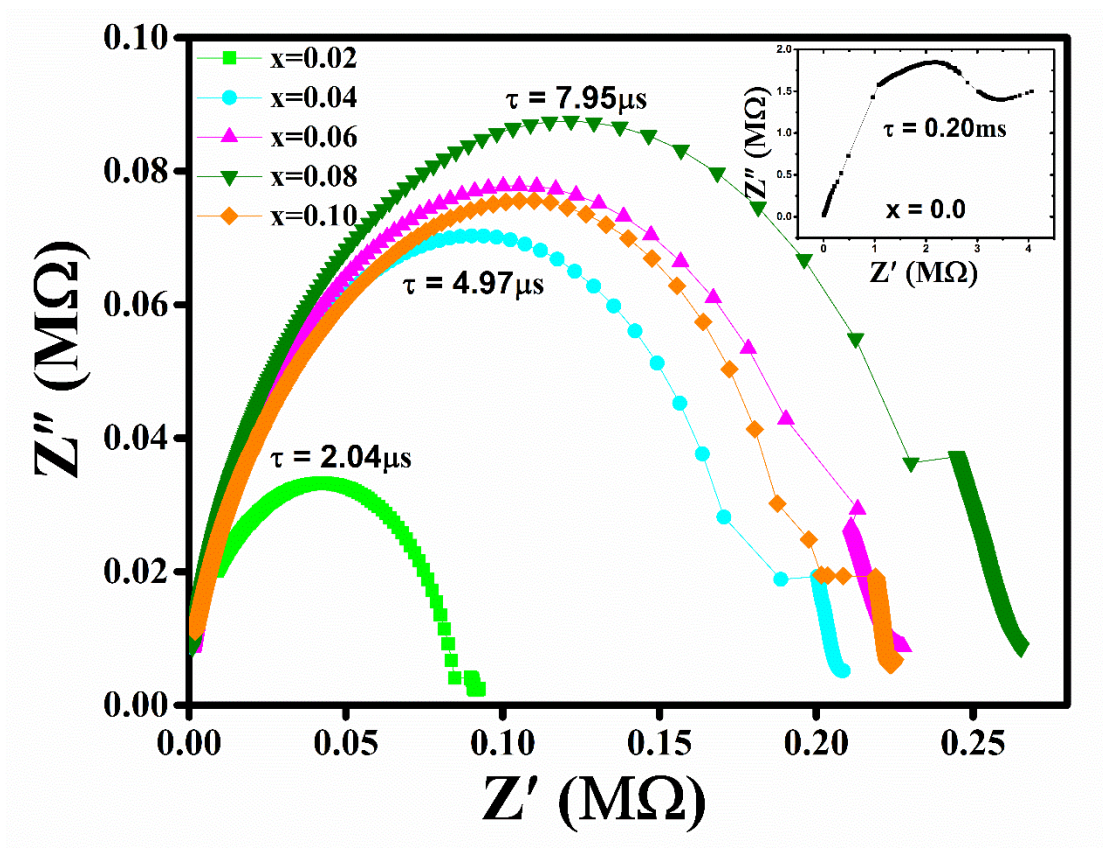


Fig.5 Nyquist plots of $\text{Bi}_2\text{Mo}_{1-x}\text{W}_x\text{O}_6$ materials

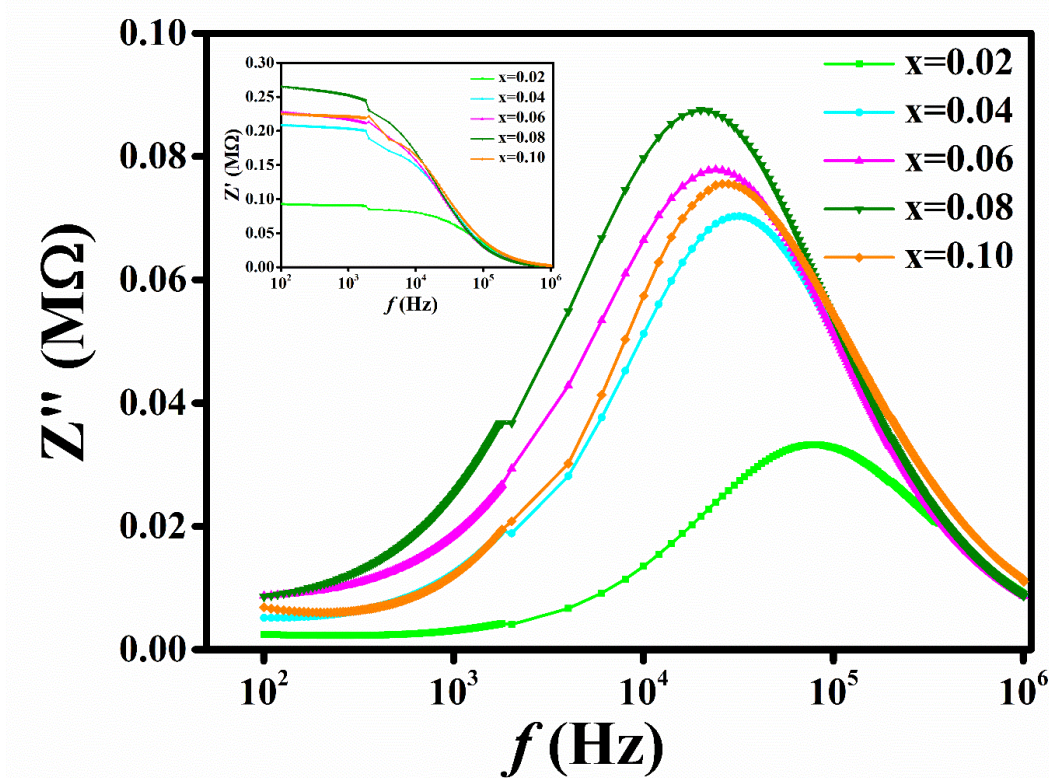


Fig.6 Frequency dispersion in real and imaginary impedance

between grains due to high capacitive reactance (X_c). Minimum height of Z'' -peak for 2% tungsten doped sample is an indicative of minimum bulk grain resistance along with resistive grain boundary. An increase in peak broadening on increasing tungsten content from 2 to 8% is an indicative of doping caused multiple relaxation that decreases as tungsten concentration is 10%. Modulus spectroscopy distinguishes grain and grain boundary capacitive contribution by suppressing electrode effect. Fig.7 shows the conclusive tungsten doping control on high frequency responsive capacitive grain boundary and low frequency responsive space charge boundaries between material and electrodes in $\text{Bi}_2\text{Mo}_{1-x}\text{W}_x\text{O}_6$ materials. Highly discontinuous (in high frequency range) pair of two semicircles for undoped Bi_2MoO_6 material shows the elimination of highly capacitive porous grain boundary formed due to microwave synthesis. Initial introduction of tungsten by 1-2% is able to dissolve this capacitive grain boundary via high solid solubility feature. As a result, only low frequency responsive space charge boundaries could survive post synthesis and short after applying high frequency fields.

Therefore, doping range 4-8% shows minimum capacitance contribution (via intercept of semicircles on M' -axis) in $\text{Bi}_2\text{Mo}_{1-x}\text{W}_x\text{O}_6$ materials compared to undoped, 2 and 10% doped ones.

Long-range mobility is the hopping mechanism of electronic conduction between grains and short-range mobility is the localized conduction through diffused and conducting grain boundaries. Modulus spectroscopy is very effective tool in distinguishing these two mechanisms. Fig.8 represents the frequency dependence of real and imaginary part of electric modulus (M' and M'') for tungsten-doped BMO materials. Real modulus (M'), for each tungsten doping step, increases with frequency and saturates to a new constant value (M_∞) at frequencies beyond 1MHz. The distribution of M_∞ -value is in correlation with effect of tungsten doping in BMO materials discussed in earlier sections, i.e., minimum for 2% doped sample and maximum for undoped and 8% doped sample. This dispersion of real modulus (M') is also an indicative of dominant grain conduction over grain boundaries due to short-range mobility of electrons/holes. Imaginary modulus (M'') for each doped BMoW material exhibits an asymmetric peak depicting two distinct regions of short-range mobility (localized conduction) and long-range (hopping conduction) mobility of charge carriers. Below peak, it is the range in which charge carriers are mobile over long distances and beyond peak value, these are

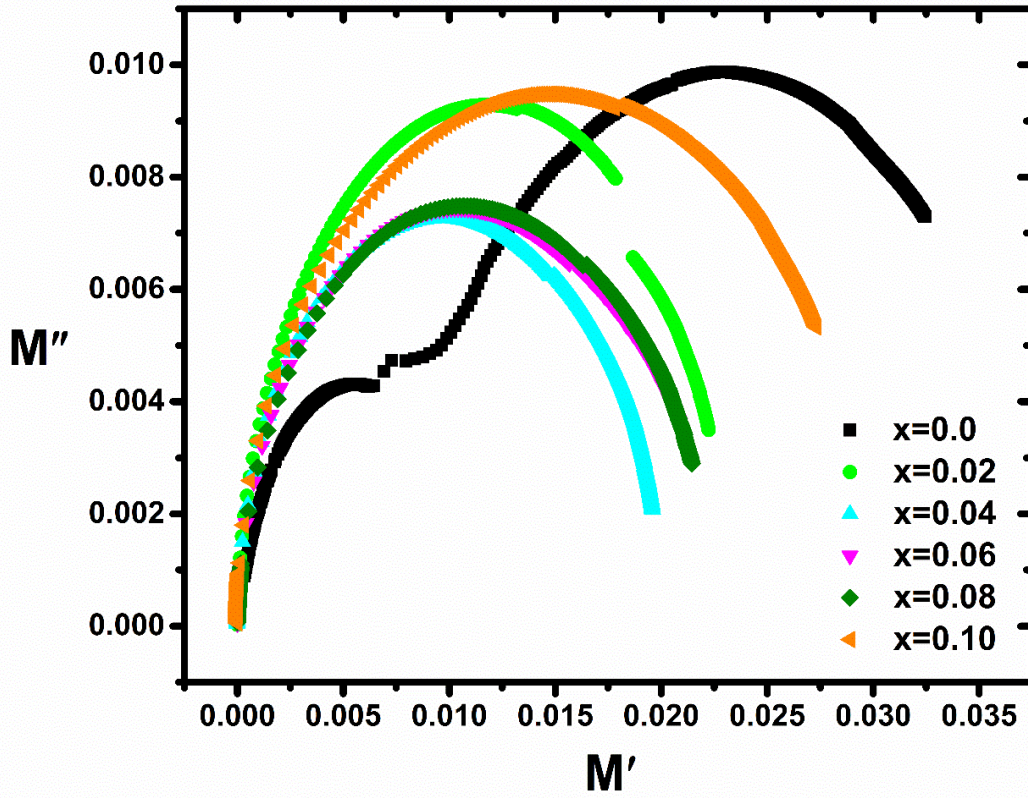


Fig.7 Frequency dependence of real (M') and imaginary part (M'') of electric modulus

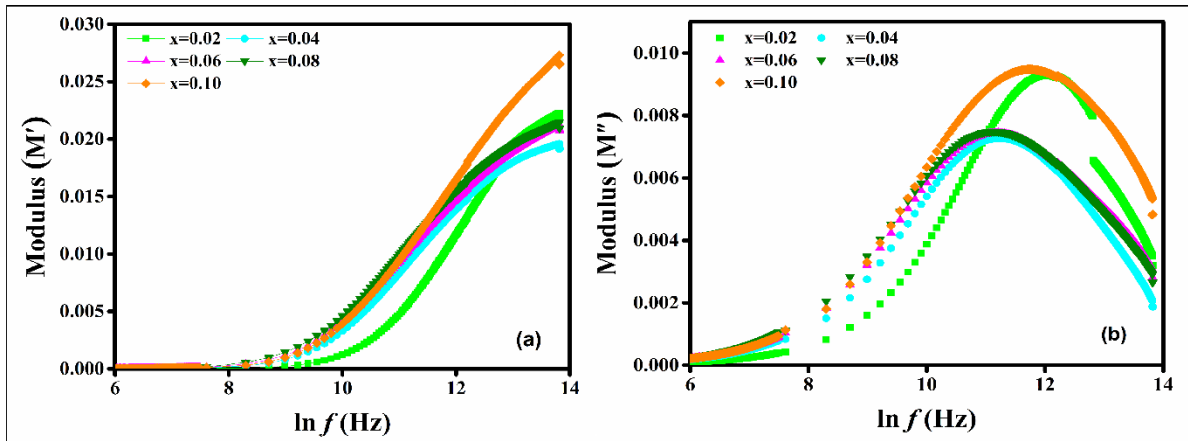


Fig.8 Frequency dependence of real (M') and imaginary part (M'') of electric modulus

confined in atomic potential wells to move for short distances. Undoped BMO material exhibits long-range mobility due to microwave synthesis derived schematic pore distribution, Fig.S1. Tungsten doping $\sim 1-2\%$ is capable to diffuse the pore formation and arrange short-

range mobility for electrons and holes. Therefore, non-Debye behaviour (hopping behaviour) of undoped BMO is effectively suppressed by tungsten doping in low range from 1-2%.

Non-capacitive Nernstian charge storage mechanism is clearly seen in BMO_W electrodes, Fig.9. Typical BMO_W compositions, undoped BMO and 10% W-doped BMO are modified using glassy carbon electrode (GCE) by dissolving 5 mM Fe(CN)₆^{3-/4-} redox couple in 0.1 M KCl. The comparison of peak currents ratio along with peak potential difference confirms an increase in reversibility of tungsten doped BMO faradaic system [BMO (I_o/I_r = 0.97, ΔE_p = 0.1510 V); BMO_W (I_o/I_r = 1.05, ΔE_p = 0.1806 V)]. Such an increase in peak potential difference is due to decreased rate constants (k_{red}/k_{ox}) depending upon Gibbs free energy change (ΔG) and excess redox potential (V):

$$k_{red} = Z \exp \frac{-\Delta G_{red}^{V=0}}{k_B T} \exp \frac{-\alpha F V}{k_B T}$$

$$k_{ox} = Z \exp \frac{-\Delta G_{ox}^{V=0}}{k_B T} \exp \frac{-(1-\alpha) F V}{k_B T}$$

where other symbols have their usual meaning (Ref). Decrease in peak current on introducing tungsten in Bi₂MoO₆ composition is due to reduction in concentration of redox molecules though generation of unsaturated charge centres for higher valence states (+3/+4) is seen. This is estimated through minor increase in anodic current around 0.75V. Charge transfer resistance (R_{ct}) of an electrode is known to decrease on increasing redox molecule concentration; the same is confirmed by comparing radius of Nyquist plot for undoped BMO sample with that of BMO_{W0.10} sample as shown in Fig.7. Lower radius of plot for undoped BMO sample compared to BMO_{W0.10} sample confirms low charge transfer resistance (R_{ct}) hence large redox current. Tungsten modified GCE/BMO_{W0.10} sample compared to GCE/undoped BMO is two-electron transfer compared to single electron transfer in BMO. The

ratio of the anodic to cathodic peak currents is lower in BMo electrode due to nearly all molybdenum ions (reducing) getting consumed in the subsequent chemical reaction, resulting in fewer atoms to oxidize during anodic scan. On the other hand, tungsten (in BMoW_{0.10}) reduces by accepting charge from Fe²⁺, Fe³⁺ and Fe⁴⁺ ions due to vacant *d*-orbital structure and oxidizes accordingly for more atomic sites during anodic scan.

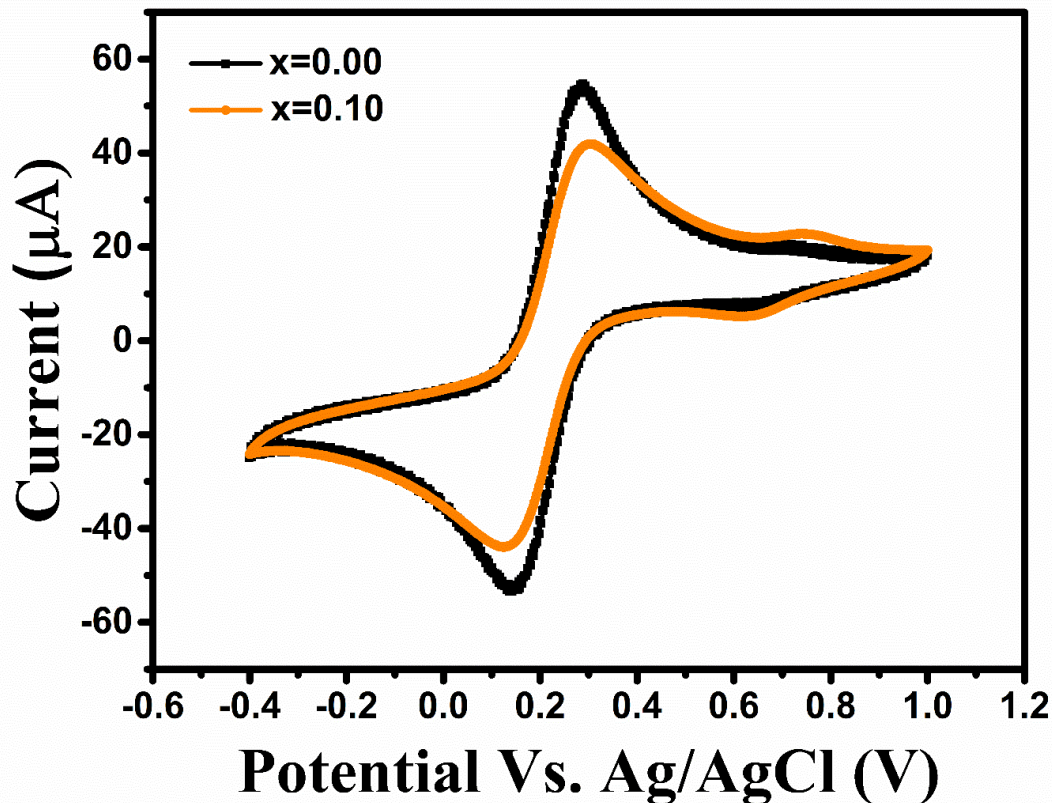


Fig.9 Multiple redox regions in tungsten doped Bi₂Mo_{1-x}W_xO₆ material

Impedance spectroscopic data as shown in Fig.5 confirms inherent oxide ion conduction dominance in Bi₂MoO₆ material (Ref-Ref-Ref). Low frequency spike emerging prominently in case of undoped Bi₂MoO₆ sample is an indicative of oxygen ion migration in lattice. Tungsten doping curtails the length of this spike significantly and converts into a low radius semi-circular arc. This is very interesting to notice that generation of freely migrating oxygen ions in Bi³⁺-Mo⁶⁺ networked lattice get limited to outer surfaces only in Bi³⁺-Mo⁶⁺-W⁶⁺ networking. This restructuring of spike into semi-circular arc to drive dominating electronic

conduction over ionic conduction is at its best for 2% tungsten doping. This provides a hint of pre-existing 2% bismuth vacancies in Bi_2MoO_6 material those are being saturated on tungsten doping. Doping of tungsten beyond 2% keeps the semi-circular form of spike maintained though with slightly increased radius under reduced height. This is an indicative of resistive-capacitive grain boundary formation away from diffusion derived Warburg resistance on electrode-grain boundary also concluded in discussion on fig.7. A few authors interpret appearance of dominating Warburg resistance in Bi_2MoO_6 material due to anisotropic thermal response of Mo-O bonds in low temperature range for increasing conducting [Ref-R.Murugan Physica B]. DC conductivity values as listed in table-3 support the interpretation on Fig.5 and further supplement the understating of electronic conduction building over oxygen ion conduction in $\text{Bi}_2\text{Mo}_{1-x}\text{W}_x\text{O}_6$ materials. Multiple activation zones can be seen in dc conductivity response of $\text{Bi}_2\text{Mo}_{1-x}\text{W}_x\text{O}_6$ materials determining role of tungsten doping in easing electron transfer, fig.10. Nearly single linear response is obtained for 6-8% tungsten doping; this confirms maximized ease in electron transfer in wide thermal range from 25°C to 300°C. However, distinctly seen two and three linear regions are recorded for other low doped $\text{Bi}_2\text{Mo}_{1-x}\text{W}_x\text{O}_6$ materials. These regions exhibit emergence of thermal actuation beyond 120°C and possessing inflexions beyond 180°C. The activation energies are calculated from Arrhenius plots and are reported corresponding to inflexion point in Table-3. The reason of different activation regimes has been interpreted earlier in terms of blocking oxygen ion transport in $\text{Bi}_2\text{Mo}_{1-x}\text{W}_x\text{O}_6$ lattice. High activation energy is due to the high polarizability of Bi^{3+} cations due to lone pair of electrons those occupy free space associated with the O^{2-} anion and hinder its (O^{2-}) movement in its sub-lattice under dc/ac fields.

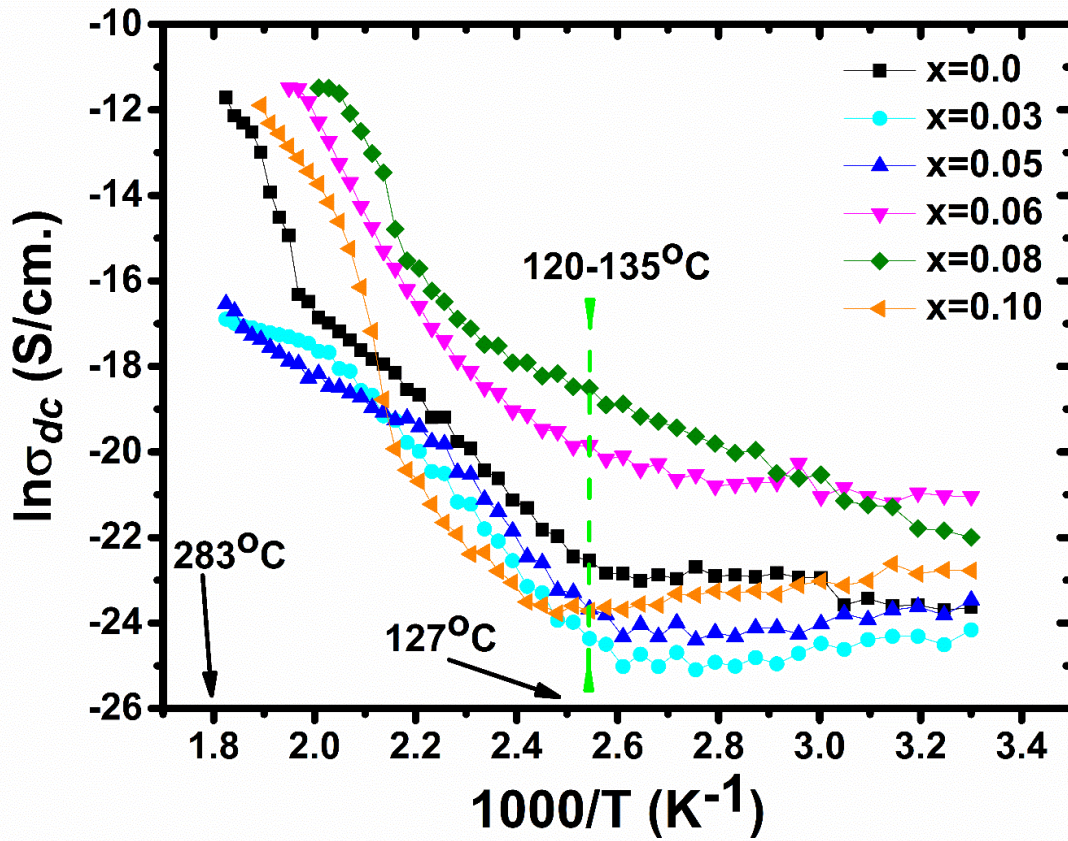


Fig.10 Multiple thermal activation zones in tungsten doped Bi_2MoO_6 materials

Table. 3 shows the variation of the electrical and optical energy band gaps for $\text{Bi}_2\text{Mo}_{1-x}\text{W}_x\text{O}_6$ materials

Tungsten doping (%)	σ_{dc} at 25°C ($\times 10^{-12}$ S/cm.)	σ_{dc} at 50°C ($\times 10^{-12}$ S/cm.)	σ_{dc} at 250°C ($\times 10^{-6}$ S/cm.)	Electrical energy band gap (eV)	
				135-180°C	180-280°C
0	54.40	66.76	0.89	0.95	2.32
3	32.05	25.56	0.033	1.12	0.27
5	64.09	40.69	0.023	1.10	0.61
6	726.14	731.08	10.23	0.66	1.89
8	279.66	594.93	10.30	0.44	2.27
10	128.33	101.49	4.48	1.13	1.43

Electronic states of low-doped $\text{Bi}_2\text{Mo}_{1-x}\text{W}_x\text{O}_6$ materials are characterized by extremely useful uv -diffuse reflectance spectroscopy in an integrated sphere mode. Non-parallel response of all absorption curves is an evidence of existing band to defect energy states transition in addition to band-to-band transition. Initial blue shift in absorption edge on increase in tungsten doping until 6% is because of merging defect energy states in conduction band edge rendering a larger optical energy gap. Doping beyond 6% generates additional energy states due to increase in polarizability and scattering effects. Optical bandgap energies are calculated using Kubelka-Munk function: $(\alpha h\nu)^n = A(h\nu - E)$, where α , h , ν , E and A are absorption coefficient, Planck's constant, frequency of electromagnetic radiation, band gap energy and a medium dependent constant respectively. Here, n determines the direct ($n=2$) or indirect ($n=1/2$) band transition characteristic of the materials. $\text{Bi}_2\text{Mo}_{1-x}\text{W}_x\text{O}_6$ materials show direct band gap transition based on linear response between $(\alpha h\nu)^2$ and $h\nu$ ($Tauc$ plots). All energy gaps are in the range 2.48-2.75 eV, such a 10% variation is very well within acceptable range according to tungsten doping concentration, Table-3. Also, the values of absorption edge onset and optical energy band gap for current microwave processed $\text{Bi}_2\text{Mo}_{1-x}\text{W}_x\text{O}_6$ materials have close

Table-4 Variation of optical energy band gap tungsten-doped $\text{Bi}_2\text{Mo}_{1-x}\text{W}_x\text{O}_6$ materials

Tungsten Doping (%)	Onset of absorption edge (nm)	Optical Energy Band gap (eV)
0	494.7	2.485
2	494.5	2.516
4	493.8	2.558
6	487.4	2.563
8	492.5	2.747

10	494.5	2.546
----	-------	-------

resemblance with nanocrystalline Bi_2MoO_6 materials prepared by solvothermal route [Ref-Actamaterialia]. Minor transition peak around 220nm is between additional energy states created for bismuth lone pair electrons that disappears completely at optimized tungsten doping level of 6% [Ref.].

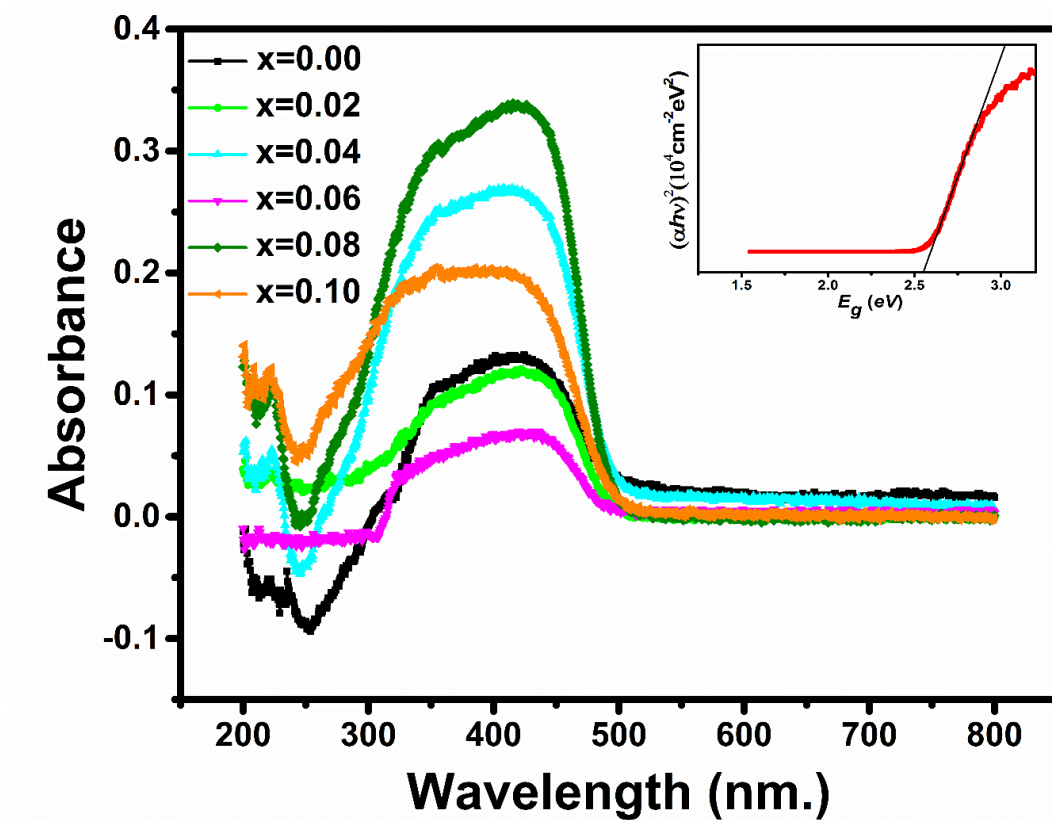


Fig.11 UV-vis diffuse absorption spectra of $\text{Bi}_2\text{Mo}_{1-x}\text{W}_x\text{O}_6$ (inset depicts typical bandgap calculation using Tauc method for $x=0.04$ sample)

4. Conclusions

The polycrystalline Bismuth molybdates are prepared from conventional solid-state route method and its Rietveld refinement reveals the orthorhombic crystal structure with space group $P2_1/C$. A gradual increase in the band gap of BMO is observed with the introduction of tungsten in the system and this increase is also suggested by the increased activation energy.

Raman data suggest the structural changes in BMO is basically due to the distortion of MoO₆ octahedra. All this study suggest that BMO can be effectively used as a photocatalyst. The polycrystalline Bismuth molybdates is prepared from conventional solid-state route method and its Rietveld refinement reveals the orthorhombic crystal structure with space group P2₁/C. An increase in *dc* activation energy is observed with incorporation of W⁶⁺ in the system and give rise to insulating behaviour in the material. Non-Debye type behaviour with distributed relaxation time period is observed from complex impedance plot. Gradual increase in the band gap of BMO is observed with introduction of tungsten in the system and this increase is also suggested by the increasing activation energy. Raman data suggest the structural changes in BMO is basically due to distortion of MoO₆ octahedra. All this study suggest that BMO can be effectively used in sensor industry.

Acknowledgments

Authors greatly acknowledge Dr. Vasant Sathe from UGC-DAE Indore for permitting us to record Raman data and Dr. Mukesh Ranjan with Mr. Suraj K. P from FCIPT-IPR Gandhi Nagar for providing Fe-SEM images. One of the authors Anurag Pritam expresses gratitude towards the Shiv Nadar Foundation for providing research fellowship.

References

- [1] D. Zhou, H. Wang, X. Yao, L.-X. Pang, Microwave Dielectric Properties of Low Temperature Firing Bi₂Mo₂O₉ Ceramic, *J. Am. Ceram. Soc.* 91 (2008) 3419–3422.
- [2] H.R. Chen, Y.C. Lee, G.H. Chen, Y.H. Chen, Microwave dielectric properties and microstructures of Y₂O₃-doped Bi₂Mo₂O₉ ceramics, *Ferroelectrics.* 434 (2012) 137–146.
- [3] H. Takeda, T. Nishida, S. Okamura, T. Shiosaki, Crystal growth of bismuth tungstate Bi₂WO₆ by slowcooling method using borate fluxes, *J. Eur. Ceram. Soc.* 25 (2005) 2731–2734.
- [4] M. Alga, A. Ammar, R. Essalim, B. Tanouti, F. Mauvy, R. Decourt, Synthesis, sintering and electrical properties of P-doped Bi₄V₂O₁₁ ceramics, *Solid State Sci.* 7 (2005) 1173–1179.
- [5] T. Zeng, H. Yan, H. Ning, J. Zeng, M.J. Reece, Piezoelectric and ferroelectric properties of bismuth tungstate ceramics fabricated by spark plasma sintering, *J. Am. Ceram. Soc.* 92 (2009) 3108–3110.

- [6] A. Castro, P. Bégué, B. Jiménez, J. Ricote, R. Jiménez, J. Galy, New $\text{Bi}_2\text{Mo}_{1-x}\text{W}_x\text{O}_6$ solid solution: Mechano-synthesis, structural study, and ferroelectric properties of the $x = 0.75$ Member, *Chem. Mater.* 15 (2003) 3395–3401.
- [7] V.I. Voronkova, E.P. Kharitonova, O.G. Rudnitskaya, Refinement of Bi_2WO_6 and Bi_2MoO_6 polymorphism, *J. Alloys Compd.* 487 (2009) 274–279.
- [8] S.K. Manik, S.K. Pradhan, Microstructure characterization of ball milled prepared nanocrystalline perovskite CaTiO_3 by Rietveld method, *Mater. Chem. Phys.* 86 (2004) 284–292.
- [9] L.N. Song, L. Chen, J. He, P. Chen, H.K. Zeng, C.T. Au, S.F. Yin, The first synthesis of Bi self-doped Bi_2MoO_6 - $\text{Bi}_2\text{Mo}_3\text{O}_{12}$ composites and their excellent photocatalytic performance for selective oxidation of aromatic alkanes under visible light irradiation, *Chem. Commun.* 53 (2017) 6480–6483.
- [10] V. Shrivastava, A. Pritam, A. Joshi, Integrating third phase transition and CO/CO contamination in microwave tailored $\text{Bi}_2\text{Mo}_{1-x}\text{W}_x\text{O}_6$ nano materials, *J. Mater. Sci. Mater. Electron.* 29 (2018) 17388–17396.
- [11] A. Fajar, E. Kartini, H. Mugirahardjo, M. Ihsan, Crystallite Size and Microstrain Measurement of Cathode Material after Mechanical Milling using Neutron Diffraction Technique, *Atom Indones.* 36 (2010) 111–115.
- [12] P. Mertens, M. Sindou, Traitement Neurochirurgical De La Spasticite Par Interventions Ablatives Au Niveau Des Racines Spinales Et De La Moelle Epiniere, *Ann. Readapt. Med. Phys.* 36 (1993) 343–347.
- [13] T. Rentschler, Substitution of lead into the bismuth oxide layers of the $n = 2$ - and $n = 3$ -Aurivillius phases, *Mater. Res. Bull.* 32 (1997) 351–369.
- [14] M. Long, W. Cai, H. Kisch, Photoelectrochemical properties of nanocrystalline Aurivillius phase Bi_2MoO_6 film under visible light irradiation, *Chem. Phys. Lett.* 461 (2008) 102–105.
- [15] V. Kumar, S. Kumari, P. Kumar, M. Kar, L. Kumar, Structural analysis by rietveld method and its correlation with optical properties of nanocrystalline zinc oxide, *Adv. Mater. Lett.* 6 (2015) 139–147.
- [16] I.C. Nogueira, L.S. Cavalcante, P.F.S. Pereira, M.M. de Jesus, J.M. Rivas Mercury, N.C. Batista, M.S. Li, E. Longo, Rietveld refinement, morphology and optical properties of $(\text{Ba}_{1-x}\text{Sr}_x)\text{MoO}_4$ crystals, *J. Appl. Crystallogr.* 46 (2013) 1434–1446.
- [17] D. Nelis, J.M. Calderon-Moreno, M. Popa, M.K. van Bael, J. Mullens, L.C. van Poucke, Formation and micro-Raman spectroscopic study of Aurivillius and fluorite-type $\text{SrBi}_2\text{Nb}_2\text{O}_9$ nanocrystallites obtained using an “amorphous citrate” route, *J. Eur. Ceram. Soc.* 26 (2006) 409–415.
- [18] L. Zhou, M. Yu, J. Yang, Y. Wang, C. Yu, Nanosheet-based $\text{Bi}_2\text{Mo}_x\text{W}_{1-x}\text{O}_6$ solid solutions with adjustable band gaps and enhanced visible-light-driven photocatalytic activities, *J. Phys. Chem. C.* 114 (2010) 18812–18818.
- [19] P.R. Scott, J.A. Crow, M. MacZka, M.B. Kruger, An X-ray diffraction study of pressure-induced phase transitions in Bi_2MoO_6 , *J. Solid State Chem.* 194 (2012) 15–18.
- [20] B.J. Kennedy, Structure of $\text{ABi}_2\text{Nb}_2\text{O}_9$ (A, Sr, Ba): Refinement of Powder Neutron Diffraction Data, *J. Solid State Chem.* 141 (2006) 135–141.
- [21] H. Li, C. Liu, K. Li, H. Wang, Preparation, characterization and photocatalytic properties of nanoplate Bi_2MoO_6 catalysts, *J. Mater. Sci.* 43 (2008) 7026–7034.
- [22] J.M. Hartmanová, M. T. Le, I. Van Driessche, S. Hoste, and F. Kundracik, Phase Composition and Charge Transport in Bismuth Molybdates. *Russian Journal of Electrochemistry*, (2005) 455-460

- [23] M. MacZka, P.T.C. Freire, C. Luz-Lima, W. Paraguassu, J. Hanuza, J. Mendes Filho, Pressure-induced phase transitions in ferroelectric Bi₂MoO₆ - A Raman scattering study, *J. Phys. Condens. Matter.* 22 (2010).
- [24] R. Murugan, Investigation on ionic conductivity and raman spectra of γ -Bi₂MoO₆, *Phys. B Condens. Matter.* 352 (2004) 227–232.
- [25] M. Zhang, C. Shao, P. Zhang, C. Su, X. Zhang, P. Liang, Y. Sun, Y. Liu, Bi₂MoO₆ microtubes: Controlled fabrication by using electrospun polyacrylonitrile microfibers as template and their enhanced visible light photocatalytic activity, *J. Hazard. Mater.* 225–226 (2012) 155–163.
- [26] G. Tian, Y. Chen, W. Zhou, K. Pan, Y. Dong, C. Tian, H. Fu, Facile solvothermal synthesis of hierarchical flower-like Bi₂MoO₆ hollow spheres as high performance visible-light driven photocatalysts, *J. Mater. Chem.* 21 (2011) 887–892.
- [27] J. Bi, L. Wu, J. Li, Z. Li, X. Wang, X. Fu, Simple solvothermal routes to synthesize nanocrystalline Bi₂MoO₆ photocatalysts with different morphologies, *Acta Mater.* 55 (2007) 4699–4705.
- [28] H. Xie, D. Shen, X. Wang, G. Shen, Microwave hydrothermal synthesis and visible-light photocatalytic activity of γ -Bi₂MoO₆ nanoplates, *Mater. Chem. Phys.* 110 (2008) 332–336.
- [29] Y. Chen, G. Tian, Y. Shi, Y. Xiao, H. Fu, Hierarchical MoS₂/Bi₂MoO₆ composites with synergistic effect for enhanced visible photocatalytic activity, *Appl. Catal. B Environ.* 164 (2015) 40–47.
- [30] D. Banerjee, A. Barman, S. Deshmukh, C.P. Saini, G. Maity, S.K. Pradhan, M. Gupta, D.M. Phase, S.S. Roy, A. Kanjilal, Oxygen mediated phase transformation in room temperature grown TiO₂ thin films with enhanced photocatalytic activity, *Appl. Phys. Lett.* 113 (2018) 084103.
- [31] Y. Sen Xu, W. De Zhang, Anion exchange strategy for construction of sesame-biscuit-like Bi₂O₂CO₃/Bi₂MoO₆ nanocomposites with enhanced photocatalytic activity, *Appl. Catal. B Environ.* 140–141 (2013) 306–316.